LETTER

Experimental observation of Bethe strings

Zhe Wang[1,2], Jianda Wu[3]†, Wang Yang[3], Anup Kumar Bera[4,5], Dmytro Kamenskyi[6], A. T. M. Nazmul Islam[4], Shenglong Xu[3], Joseph Matthew Law[7], Bella Lake[4,8], Congjun Wu[3] & Alois Loidl[1]

Almost a century ago, string states—complex bound states of magnetic excitations—were predicted to exist in one-dimensional quantum magnets[1]. However, despite many theoretical studies[2–11], the experimental realization and identification of string states in a condensed-matter system have yet to be achieved. Here we use high-resolution terahertz spectroscopy to resolve string states in the antiferromagnetic Heisenberg–Ising chain SrCo$_2$V$_2$O$_8$ in strong longitudinal magnetic fields. In the field-induced quantum-critical regime, we identify strings and fractional magnetic excitations that are accurately described by the Bethe ansatz[1,3,4]. Close to quantum criticality, the string excitations govern the quantum spin dynamics, whereas the fractional excitations, which are dominant at low energies, reflect the antiferromagnetic quantum fluctuations. Today, Bethe's result[1] is important not only in the field of quantum magnetism but also more broadly, including in the study of cold atoms and in string theory; hence, we anticipate that our work will shed light on the study of complex many-body systems in general.

Magnons are elementary quasiparticle excitations above the ground state in ferromagnets, which govern the low-temperature thermodynamics[4]. For excited states with two or more magnons, a description in terms of free quasiparticles is very incomplete, especially in one and two dimensions, because the magnons can form bound states that share centre-of-mass momenta owing to the exchange interactions[12]. For a one-dimensional system, bound states of magnons can be viewed as magnetic solitons[13] in the classical limit, which correspond to strings of flipped spins that exist as bound entities in the chain. Studying the dynamical properties of interacting magnetic excitations is of interest not only because of the potential applications in quantum information[14], but also because it could provide insight into fundamental aspects of quantum magnetism and quantum many-body systems[15].

In the one-dimensional spin-1/2 Heisenberg model—a paradigmatic model of interacting spin systems—the existence of bound states was first predicted in the early 1930s by Bethe for two magnons[1]. The systematic ansatz introduced by Bethe for calculating the eigenvalues and eigenstates of the Heisenberg model exactly was later generalized to the description of multi-magnon bound states—the so-called Bethe strings—in models beyond the isotropic limit[3,4,6,8,9]. It is generally believed that spin dynamics is governed by low-energy multi-particle excitations[7,16–19]; however, the excitations of two-magnon bound states (two-string states) have recently been theoretically suggested to be dominant in the isotropic Heisenberg antiferromagnet[10]. Nevertheless, the string excitations are sensitive to exchange anisotropy: for an easy-plane anisotropy, although the spin excitations remain gapless, the dynamical response of string states is substantially smaller compared with the fractional multi-particle excitations (spinons)[8,9]. In addition, in a spin-gapped Heisenberg–Ising antiferromagnet with easy-axis anisotropy, the dynamical properties are dominated by the fractional spinon excitations[19,20]. Hence, experimentally realizing string states is very difficult, and has yet to be achieved in condensed-matter

systems. Here, we perform terahertz spectroscopy on the one-dimensional Heisenberg–Ising antiferromagnetic system SrCo$_2$V$_2$O$_8$ in longitudinal magnetic fields. We show that when the spin gap is closed

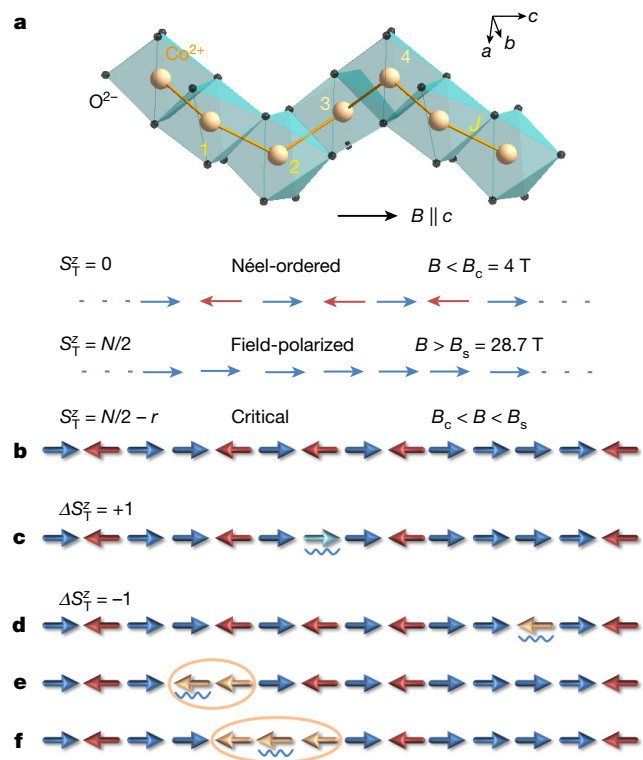**Figure 1 | Quantum spin chain in SrCo$_2$V$_2$O$_8$, psinon–(anti)psinon pairs and strings.** Psinon–(anti)psinon pairs and strings are the characteristic magnetic excitations in one dimension in the critical regime. **a**, Chain structure of SrCo$_2$V$_2$O$_8$ with a four-fold screw axis along the c direction. At 1.7 K, Néel-ordered ($S_T^z = 0$) and field-polarized ($S_T^z = N/2$) states are stabilized for longitudinal magnetic fields $B < B_c = 4$ T and $B > B_s = 28.7$ T, respectively, where the spins are represented by the arrows. **b**, A representative configuration of the ground state in the critical regime ($B_c < B < B_s$) for total spin-z quantum number $S_T^z = N/2 - r$ with r flipped spins with respect to the fully polarized state. **c–f**, Excitations above the ground state are allowed by the selection rules $\Delta S_T^z = +1$, yielding psinon–psinon pairs (**c**), and $\Delta S_T^z = -1$, yielding psinon–antipsinon pairs (**d**), two-string states (**e**) or three-string states (**f**), which govern the interaction with the magnetic field of a photon. Whereas the psinon–(anti)psinon pairs can propagate throughout the chain without forming bound states, the two-string and three-string states (bound states formed by two and three magnons, respectively; circled) move as entities in the chain. The flipped spin with respect to the ground state (**b**) is indicated by a wiggly line for each excited state (**c–f**).

[1]Experimental Physics V, Center for Electronic Correlations and Magnetism, Institute of Physics, University of Augsburg, 86135 Augsburg, Germany. [2]Institute of Radiation Physics, Helmholtz-Zentrum Dresden-Rossendorf, 01328 Dresden, Germany. [3]Department of Physics, University of California, San Diego, California 92093, USA. [4]Helmholtz-Zentrum Berlin für Materialien und Energie, 14109 Berlin, Germany. [5]Solid State Physics Division, Bhabha Atomic Research Centre, Mumbai 400085, India. [6]High Field Magnet Laboratory, Radboud University, 6525 ED Nijmegen, The Netherlands. [7]Hochfeld Magnetlab Dresden, Helmholtz-Zentrum Dresden-Rossendorf, 01314 Dresden, Germany. [8]Institut für Festkörperphysik, Technische Universität Berlin, 10623 Berlin, Germany. †Present address: Max-Planck-Institut für Physik komplexer Systeme, 01187 Dresden, Germany.
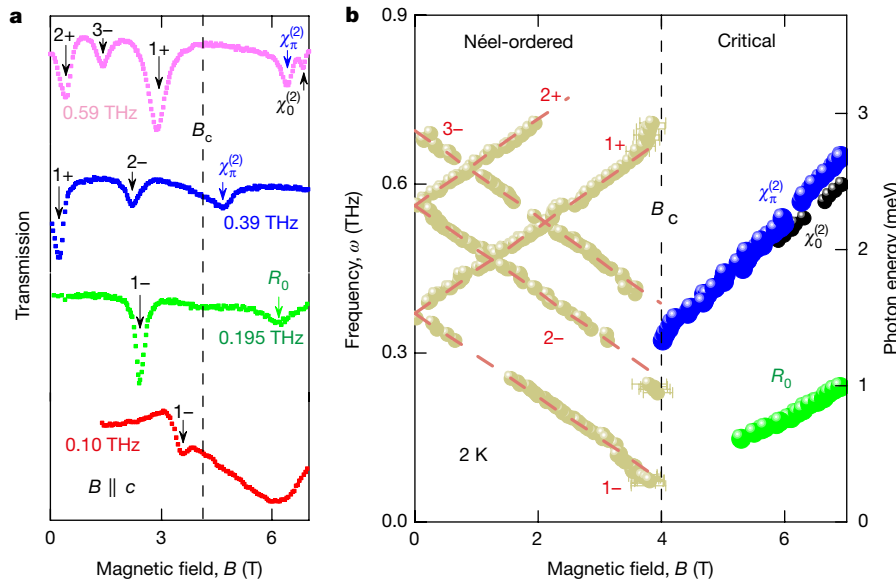
Figure 2 | Softening of spinons and emergent magnetic excitations at the quantum phase transition in SrCo$_2$V$_2$O$_8$. a, Transmission spectra of magnetic excitations in SrCo$_2$V$_2$O$_8$ for various frequencies below 1 THz, measured with the applied longitudinal magnetic field $B \parallel c$ and the electromagnetic wave propagating along the c axis. Magnetic resonance excitations corresponding to transmission minima are indicated by arrows. **b**, Eigenfrequencies of the resonance modes as a function of the applied magnetic field. For $B < B_c$, a series of confined fractional spinon

excitations split in low fields ($1\pm$, $2\pm$, …) and follow a linear field dependence (dashed lines). Above B_c, new modes emerge (R_0, $\chi_0^{(2)}$ and $\chi_\pi^{(2)}$) with completely different field dependencies. Deviations from the linear field dependence appear when approaching the critical field. Error bars indicate the resonance line widths. In both panels, the field-induced phase transition from the Néel-ordered phase to the critical regime is indicated by the vertical dashed line at the critical field $B_c = 4$ T.

above a field-induced quantum phase transition at $B_c = 4$ T, many-body two-string and three-string states are identified in the quantum-critical regime before a fully field-polarized state is reached at $B_s = 28.7$ T. On decreasing the magnetic field from B_s, the dominant role of the low-energy fractional multi-particles in the dynamical response is gradually taken over by the string states, which govern the quantum spin dynamics close to the quantum phase transition.

The realization of the one-dimensional Heisenberg–Ising model in SrCo$_2$V$_2$O$_8$ is based on its crystal structure and the dominant nearest-neighbour antiferromagnetic interactions (Fig. 1a). The screw chains of CoO$_6$ octahedra, with the four-fold screw axis running along the crystallographic c direction, are arranged in a tetragonal structure. Owing to spin–orbit coupling, the atomic magnetic moments of the Co^{2+} ions, comprising the spin and orbital degrees of freedom, are exposed to an Ising anisotropy. The crystal electric field in the CoO$_6$ octahedra lifts the twelve-fold degeneracy of the Co^{2+} moments, which results in a Kramers doublet ground state with a total angular momentum of 1/2 (ref. 21). Magnetization and neutron diffraction experiments reveal that the Ising anisotropy forces the atomic magnetic moments along the c axis, with Néel-type collinear antiferromagnetic order stabilized below $T_N = 5$ K (ref. 22).

Superexchange interactions between the magnetic moments in the chains of SrCo$_2$V$_2$O$_8$ are described by the Hamiltonian of the one-dimensional spin-1/2 Heisenberg–Ising model[23,24]:

$$H = J \sum_{n=1}^{N} [(S_n^x S_{n+1}^x + S_n^y S_{n+1}^y) + \Delta S_n^z S_{n+1}^z] - g_\parallel \mu_B B \sum_{n=1}^{N} S_n^z$$

where $J > 0$ is the antiferromagnetic coupling between neighbouring spins, $\Delta > 1$ accounts for the Ising anisotropy between the longitudinal and transverse spin couplings, $S_n^{x,y,z}$ are the spin components at the nth site and N is the length of the chain. The last term corresponds to the Zeeman interaction in a longitudinal magnetic field B along the c axis with g-factor $g_\parallel$ and Bohr magneton μ_B.

The Néel ground state at zero field can be illustrated by an antiparallel alignment of neighbouring spins, corresponding to a total spin-z quantum number of $S_T^z = 0$ (Fig. 1a). One spin flip creates an

excitation of two spinons[20], which can propagate separately along the chain via subsequent spin flips. In momentum space the spinons form a two-particle excitation continuum[16–19] that is gapped above the antiferromagnetic ground state.

As a result of the Zeeman interaction, a longitudinal magnetic field can reduce and finally close the spin gap at a critical field B_c (ref. 2). Before reaching the fully polarized state ($B > B_s$; Fig. 1a) in which the elementary excitations are gapped magnons, the system enters a gapless phase that corresponds to the critical regime ($B_c < B < B_s$). A general ground state in this regime with an arbitrary value of S_T^z is illustrated in Fig. 1b, and fundamentally new and exotic states can be excited by flipping a single spin (Fig. 1c–f). According to the Bethe ansatz[1], the spin excitations in the critical regime can be bound states of n magnons (n-string states)[3,4] or low-energy spinon-like quasiparticles[5,7–10]. The spinon-like quasiparticles, which form multi-particle continua[25] similarly to spinons (see Methods), are named psinons or antipsinons[7,8] in the context of the Bethe ansatz to distinguish them from the spinons in zero field. We adopt this nomenclature in the following for this reason and, more importantly, because our results reveal that the excitations of psinon–psinon and psinon–antipsinon pairs obey different selection rules (Fig. 1c, d).

Because excitations with $\Delta S_T^z = +1$ and $\Delta S_T^z = -1$ are both allowed by the selection rules that govern the interaction with the magnetic field of photons or with the magnetic moment of neutrons, the excited states illustrated in Fig. 1c–f should be observable in optical or neutron-scattering experiments. We use terahertz optical spectroscopy on the Heisenberg–Ising antiferromagnetic chain SrCo$_2$V$_2$O$_8$ in a longitudinal magnetic field up to 30 T. Our results provides clear experimental evidence for the existence of the many-body two-string and three-string states and of the fractional multi-particle excitations that characterize the quantum spin dynamics of the one-dimensional spin-1/2 Heisenberg–Ising model.

In a longitudinal magnetic field, S_T^z is a good quantum number. The eigenstates of the Heisenberg–Ising model can therefore be classified accordingly, and described by a general Bethe-ansatz wavefunction

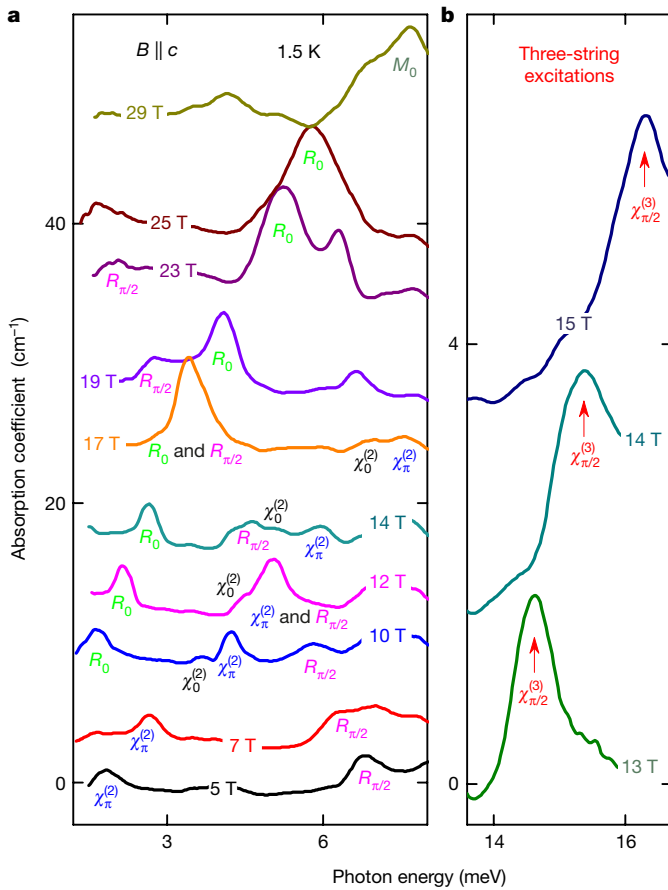$$|\varphi\rangle = \sum_{1 \leq n_1 < \cdots < n_r \leq N} a(n_1, n_2, \ldots, n_r)|n_1, n_2, \ldots, n_r\rangle$$

Figure 3 | Absorption spectra of psinon–psinon, psinon–antipsinon, two-string and three-string excitations for $B_c < B < B_s$ and of magnons for $B > B_s$ in SrCo$_2$V$_2$O$_8$. a, b, Absorption spectra for various longitudinal magnetic fields in the critical regime in the low-energy (**a**) and high-energy (**b**) spectral ranges. **a,** Four types of excitation—R_0, $R_{\pi/2}$, $\chi_0^{(2)}$ and $\chi_\pi^{(2)}$, each with a characteristic field dependence—are observed in the critical regime ($B_c < B < B_s$). Mode R_0 evolves from mode M_0 above B_s. Whereas mode $R_{\pi/2}$ softens with increasing fields, the eigenenergies of the other modes increase. **b,** A higher-energy mode ($\chi_{\pi/2}^{(3)}$) can be resolved at relatively low magnetic fields. The spectra are shifted upwards proportional to the corresponding magnetic fields.

for a total spin-z quantum number $S_T^z = N/2 - r$ (Fig. 1b), with N denoting the length of the chain and with r flipped spins (at sites $n_1, n_2, ..., n_r$ in the chain) with respect to the fully spin-polarized state $|\cdots \rightarrow \rightarrow \rightarrow \cdots\rangle$, that is, $|n_1, n_2, ..., n_r\rangle = S_{n_1}^- S_{n_2}^- ... S_{n_r}^- |\cdots \rightarrow \rightarrow \rightarrow \cdots\rangle$, where $S_{n_j}^\pm \equiv S_{n_j}^x \pm i S_{n_j}^y$ are the operators that flip the spin of site n_j. We use the Bethe ansatz to obtain the coefficients $a(n_1, n_2, ..., n_r)$ and the eigenenergies of the ground state and the excited states for every S_T^z (see Methods). The excited states of psinon–(anti)psinon pairs and of n-strings correspond to the real and complex momenta in the solutions of the Bethe-ansatz equations[1,3,4,6,8–11], and are labelled as R_q and $\chi_q^{(n)}$, respectively, with the subscript indexing the corresponding transfer momenta. The excitations that are allowed in optical experiments obey the selection rules $\Delta S_T^z = +1$ or $\Delta S_T^z = -1$. These excitations contribute to the dynamic structure factors $S^{-+}(q, \omega)$ or $S^{+-}(q, \omega)$, respectively, defined by

$$S^{a\bar{a}}(q, \omega) = \pi \sum_\mu \left| \langle \mu | S_q^{\bar{a}} | G \rangle \right|^2 \delta(\omega - E_\mu + E_G)$$

in which $\bar{a} = -a$ with $a \in \{+, -\}$, $|G\rangle$ and $|\mu\rangle$ are the ground and excited states, with eigenenergies of E_G and E_μ, respectively, and
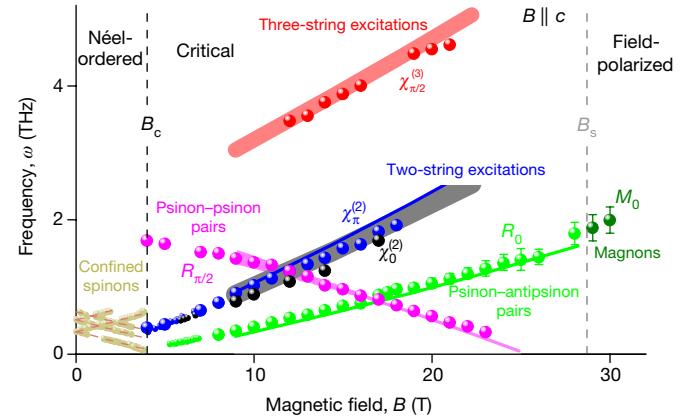
$$S_q^\pm = \frac{1}{\sqrt{N}} \sum_n e^{iqn} S_n^\pm$$

Figure 4 | Magnetic excitations in the longitudinal-field Heisenberg–Ising chain SrCo$_2$V$_2$O$_8$. Eigenfrequencies are shown as a function of longitudinal magnetic field for all magnetic excitations observed experimentally (symbols). Below $B_c = 4$ T, confined spinons are observed in the Néel-ordered phase. In the critical regime ($B_c < B < B_s$), excitations of psinon–psinon pairs ($R_{\pi/2}$ at $q = \pi/2$), psinon–antipsinon pairs (R_0 at $q = 0$), and of complex many-body two-string ($\chi_0^{(2)}$ and $\chi_\pi^{(2)}$ at $q = 0$ and $q = \pi$, respectively) and three-string ($\chi_{\pi/2}^{(3)}$ at $q = \pi/2$) bound states are identified by the field dependencies of their eigenfrequencies. Above $B_s = 28.7$ T, magnons (M_0 at $q = 0$) are observed in the field-polarized ferromagnetic phase. Solid lines display the results of the dynamic structure factors $S^{-+}(q, \omega)$ and $S^{+-}(q, \omega)$ at $q = 0$, $q = \pi/2$ and $q = \pi$ for the corresponding excitations of the one-dimensional spin-1/2 antiferromagnetic Heisenberg–Ising model. For all five modes (R_0, $R_{\pi/2}$, $\chi_0^{(2)}$, $\chi_\pi^{(2)}$ and $\chi_{\pi/2}^{(3)}$), excellent agreement between theory and experiment is achieved using an exchange interaction $J = 3.55$ meV, g-factor $g_\parallel = 6.2$ and Ising anisotropy $\Delta = 2$ (ref. 24). Experimental and theoretical line widths are indicated by error bars and shading, respectively.

Hence, we can quantitatively attribute the contributions of string excitations and psinon–(anti)psinon pairs to the relevant dynamic structure factors. The string excitations with higher energies and characteristic field dependencies can readily be distinguished from the low-energy psinon–(anti)psinon pairs (see Methods). This enables us to compare the theoretical calculations to the experimental results precisely as a function of the longitudinal field and to identify the nature of each observed mode.

In Fig. 2a we show transmission spectra at various frequencies below 1 THz as a function of longitudinal magnetic field. At 0.195 THz, two transmission minima are observed, at 2.41 T (mode 1−) and 6.18 T (mode R_0), below and above the critical field $B_c = 4$ T. With increasing magnetic fields, mode 1− shifts to lower frequencies and mode R_0 to higher frequencies. Mode 1− together with modes 1+, 2−, 2+ and 3−, which are observed at higher frequencies (0.39 THz and 0.59 THz), are known as confined spinon excitations[23] owing to the inter-chain couplings in the gapped Néel-ordered phase ($B < B_c$). Well below the critical field B_c (Fig. 2b) the confined spinons exhibit Zeeman splitting with linear field dependence[23]. Close to the critical field mode 1− softens, concomitant with a substantial hardening of mode 1+. This indicates that the inter-chain couplings are suppressed above B_c and that the system enters the field-induced critical regime in one dimension. Completely different excitation spectra appear in the critical regime: in the same frequency range (Fig. 2a), we unambiguously observe three sharp modes, denoted by R_0, $\chi_0^{(2)}$ and $\chi_\pi^{(2)}$. With increasing magnetic field well above the critical field B_c, the eigenenergies of the three modes increase linearly with different slopes (Fig. 2b).

Using magneto-optic spectroscopy in a high-field laboratory, we are able to extend the search for magnetic excitations to a much larger spectral range and to higher magnetic fields up to 30 T, covering the complete critical regime ($B_c < B < B_s$) and the field-polarized ferromagnetic phase ($B > B_s = 28.7$ T). As displayed in Fig. 3, the magnetic

excitations are represented by the peaks in the absorption-coefficient spectra at various magnetic fields. At 10 T, we identify not only modes R_0, $\chi_0^{(2)}$ and $\chi_\pi^{(2)}$ at 1.66 meV, 3.67 meV and 4.23 meV, respectively, in a sequence of increasing energies, but also a higher-energy mode $R_{\pi/2}$ at 5.82 meV. Whereas modes R_0 and $\chi_\pi^{(2)}$ have comparable absorption coefficients, mode $\chi_0^{(2)}$ is much weaker, which is consistent with the low-field measurements (such as the 0.59-THz spectrum in Fig. 2a). In higher magnetic fields, mode $R_{\pi/2}$ softens, whereas the other modes (R_0, $\chi_0^{(2)}$ and $\chi_\pi^{(2)}$) shift to higher energies. Above the low-energy phonon bands (see Methods), we resolve a further high-energy magnetic excitation $\chi_{\pi/2}^{(3)}$ of 14.6 meV at 13 T, which shifts to higher energies with increasing magnetic field (Fig. 3b). The field dependence of the eigenfrequencies of the five observed modes (R_0, $R_{\pi/2}$, $\chi_0^{(2)}$, $\chi_\pi^{(2)}$ and $\chi_{\pi/2}^{(3)}$) is summarized in Fig. 4 (symbols). The field dependencies are linear for all of the modes, each with distinct slope and characteristic energy.

From the Bethe-ansatz calculations[6], we can single out various excitations and evaluate their respective contributions to the dynamic structure factors $S^{-+}(q, \omega)$ and $S^{+-}(q, \omega)$ (Methods). In accord with Brillouin-zone folding due to the four-fold screw-axis symmetry of the spin chain[22,24], in Fig. 4 we show the peak frequencies in $S^{-+}(q, \omega)$ and $S^{+-}(q, \omega)$ as a function of magnetic field (solid lines) for the transfer momenta $q = 0$, $q = \pi/2$ and $q = \pi$, so as to compare to the terahertz spectroscopic results. Excellent agreement between theory and experiment is achieved for all five distinct magnetic excitations, which enables us to unambiguously identify their nature: R_0 characterizes psinon–antipsinon pairs at $q = 0$, whereas $R_{\pi/2}$ characterizes psinon–psinon pairs at $q = \pi/2$. The psinon–antipsinon excitations R_0, related to the single spin-flip operator $S_{q=0}^-$, evolve from the magnon mode M_0 in the field-polarized ferromagnetic phase, in which the largest absorption is observed experimentally (Figs 3a, 4). Most strikingly, we are able to detect and identify the two-string states $\chi_0^{(2)}$ and $\chi_\pi^{(2)}$ at $q = 0$ and $q = \pi$, respectively, and the three-string states $\chi_{\pi/2}^{(3)}$ for $q = \pi/2$.

The branch of psinon–psinon pairs $R_{\pi/2}$ belongs to $S^{-+}(q, \omega)$ and obeys the selection rule $\Delta S_T^z = +1$. Hence, the psinon–psinon excitations correspond to flipping one spin into the direction of the magnetic field (Fig. 1c), which will decrease the Zeeman energy, so that mode $R_{\pi/2}$ softens with increasing field. By contrast, the psinon–antipsinon pairs and the string states, which correspond to $S^{+-}(q, \omega)$, obey the selection rule $\Delta S_T^z = -1$ (Fig. 1d–f) and so their eigenenergies increase with magnetic field. The linear dependencies, which arise essentially from the linear dependence of the Zeeman energy on magnetic field, are substantially renormalized as a result of the one-dimensional many-body interactions.

The observation of three-string states reflects a very peculiar feature of the one-dimensional Heisenberg–Ising model: close to quantum criticality, even three magnons can form a stable bound state and, more surprisingly, the bound states of three magnons govern the dynamical response[26]. This is in clear contrast to the isotropic Heisenberg model, in which the two-string states dominate[10], or to the models with easy-plane anisotropy, in which the fractional multi-particles essentially characterize the dynamical properties[8,9]. Besides their eigenfrequencies, the contribution of the string states to the spin dynamics is also strongly field-dependent[8–10,26]. Starting from the quantum phase transition of the Heisenberg–Ising model[26], an increase in magnetic field leads to a decreasing contribution of the string excitations. Above the half-saturated magnetization, the low-energy multi-particle excitations become dominant, finally governing the spin dynamics in the fully field-polarized limit (Methods). This is manifested by the rapidly increasing absorption of mode R_0 (see Fig. 3).

We have identified many-body two-string and three-string states in the quantum-critical regime of a one-dimensional spin-1/2 Heisenberg–Ising chain. This represents an example of the experimental realization of strongly correlated quantum states in condensed-matter systems[27]. Further dynamical properties of the string states are expected to be revealed from inelastic neutron-scattering studies, which can probe the whole Brillouin zone also for the excitation continua[16–19,25], thus allowing a more detailed comparison to theory. The stability of the string states, as indicated by our results, provides the possibility to study their non-equilibrium behaviour in quantum magnets[28] and cold-atom lattices[29]. Thus, our results pave the way towards the deterministic manipulation of complex magnetic many-body states in solid-state materials and shed light on the study of quantum quench dynamics[11], the Hubbard model[30], and string excitations in string theory[15,31].

Online Content Methods, along with any additional Extended Data display items and Source Data, are available in the online version of the paper; references unique to these sections appear only in the online paper.

1. Bethe, H. Zur Theorie der Metalle. I. Eigenwerte und Eigenfunktionen der linearen Atomkette. *Z. Phys.* **71**, 205–226 (1931).
2. Yang, C. N. & Yang, C. P. One-dimensional chain of anisotropic spin-spin interactions. II. Properties of the ground-state energy per lattice site for an infinite system. *Phys. Rev.* **150**, 327–339 (1966).
3. Gaudin, M. Thermodynamics of the Heisenberg-Ising ring for $\Delta \geq 1$. *Phys. Rev. Lett.* **26**, 1301–1304 (1971).
4. Takahashi, M. & Suzuki, M. One-dimensional anisotropic Heisenberg model at finite temperatures. *Prog. Theor. Phys.* **48**, 2187–2209 (1972).
5. Müller, G., Thomas, H., Beck, H. & Bonner, J. C. Quantum spin dynamics of the antiferromagnetic linear chain in zero and nonzero magnetic field. *Phys. Rev. B* **24**, 1429–1467 (1981).
6. Kitanine, N., Mailet, J. M. & Terras, V. Form factors of the XXZ Heisenberg spin-1/2 finite chain. *Nucl. Phys. B* **554**, 647–678 (1999).
7. Karbach, M. & Müller, G. Line-shape predictions via Bethe ansatz for the one-dimensional spin-1/2 Heisenberg antiferromagnet in a magnetic field. *Phys. Rev. B* **62**, 14871–14879 (2000).
8. Sato, J., Shiroishi, M. & Takahashi, M. Evaluation of dynamic spin structure factor for the spin-1/2 XXZ chain in a magnetic field. *J. Phys. Soc. Jpn* **73**, 3008–3014 (2004).
9. Caux, J.-S., Hagemans, R. & Maillet, J. M. Computation of dynamical correlation functions of Heisenberg chains: the gapless anisotropic regime. *J. Stat. Mech.* **2005,** P09003 (2005).
10. Kohno, M. Dynamically dominant excitations of string solutions in the spin-1/2 antiferromagnetic Heisenberg chain in a magnetic field. *Phys. Rev. Lett.* **102**, 037203 (2009).
11. Ganahl, M., Rabel, E., Essler, F. H. L. & Evertz, H. G. Observation of complex bound states in the spin-1/2 Heisenberg XXZ chain using local quantum quenches. *Phys. Rev. Lett.* **108**, 077206 (2012).
12. Wortis, M. Bound states of two spin waves in the Heisenberg ferromagnet. *Phys. Rev.* **132**, 85–97 (1963).
13. Fogedby, H. C. The spectrum of the continuous isotropic quantum Heisenberg chain: quantum solitons as magnon bound states. *J. Phys. Chem.* **13**, L195–L200 (1980).
14. Subrahmanyam, V. Entanglement dynamics and quantum-state transport in spin chains. *Phys. Rev. A* **69**, 034304 (2004).
15. Batchelor, M. T. The Bethe ansatz after 75 years. *Phys. Today* **60**, 36–40 (2007).
16. Tennant, D. A., Perring, T. G., Cowley, R. A. & Nagler, S. E. Unbound spinons in the $S=1/2$ antiferromagnetic chain KCuF$_3$. *Phys. Rev. Lett.* **70**, 4003–4006 (1993).
17. Lake, B. *et al.* Confinement of fractional quantum number particles in a condensed-matter system. *Nat. Phys.* **6**, 50–55 (2010).
18. Mourigal, M. *et al.* Fractional spinon excitations in the quantum Heisenberg antiferromagnetic chain. *Nat. Phys.* **9**, 435–441 (2013).
19. Wu, L. S. *et al.* Orbital-exchange and fractional quantum number excitations in an *f*-electron metal, Yb$_2$Pt$_2$Pb. *Science* **352**, 1206–1210 (2016).
20. Faddeev, L. D. & Takhtajan, L. A. What is the spin of a spin wave? *Phys. Lett. A* **85**, 375–377 (1981).
21. Lines, M. E. Magnetic properties of CoCl$_2$ and NiCl$_2$. *Phys. Rev.* **131**, 546–555 (1963).
22. Bera, A. K., Lake, B., Stein, W.-D. & Zander, S. Magnetic correlations of the quasi-one-dimensional half-integer spin-chain antiferromagnets Sr*M*$_2$V$_2$O$_8$ (*M*=Co, Mn). *Phys. Rev. B* **89**, 094402 (2014).
23. Wang, Z. *et al.* Spinon confinement in the one-dimensional Ising-like antiferromagnet SrCo$_2$V$_2$O$_8$. *Phys. Rev. B* **91**, 140404 (2015).
24. Wang, Z. *et al.* From confined spinons to emergent fermions: observation of elementary magnetic excitations in a transverse-field Ising chain. *Phys. Rev. B* **94**, 125130 (2016).
25. Stone, M. B. *et al.* Extended quantum critical phase in a magnetized spin-1/2 antiferromagnetic chain. *Phys. Rev. Lett.* **91**, 037205 (2003).
26. Yang, W., Wu, J., Xu, S., Wang, Z. & Wu, C. Quantum spin dynamics of the axial antiferromagnetic spin-1/2 XXZ chain in a longitudinal magnetic field. Preprint at https://arxiv.org/abs/1702.01854 (2017).
27. Essler, F. H. L. & Konik, R. M. in *From Fields to Strings: Circumnavigating Theoretical Physics* (eds Shifman, M. *et al.*) Vol. 1, 684–830 (World Scientific, 2005).

28. Nishida, Y., Kato, Y. & Batista, C. D. Efimov effect in quantum magnets. *Nat. Phys.* **9,** 93–97 (2013).
29. Fukuhara, T. *et al.* Microscopic observation of magnon bound states and their dynamics. *Nature* **502,** 76–79 (2013).
30. Lieb, E. H. & Wu, F. Y. Absence of Mott transition in an exact solution of the short-range, one-band model in one dimension. *Phys. Rev. Lett.* **20,** 1445–1448 (1968).
31. Minahan, J. A. & Zarembo, K. The Bethe-ansatz for $\mathcal{N}=4$ super Yang-Mills. *J. High Energy Phys.* **3,** 13 (2003).

Author Contributions Z.W. conceived and performed the optical experiments, analysed the data and coordinated the project. J.W., W.Y. and S.X. carried out the Bethe-ansatz calculations. A.K.B. and A.T.M.N.I. prepared and characterized the high-quality single crystals. A.K.B. and J.M.L. performed the high-field magnetization measurements. D.K. assisted with the high-field optical experiments. B.L., C.W. and A.L. supervised the project. Z.W., J.W., W.Y., C.W. and A.L. wrote the manuscript with input from all authors. All authors discussed the results.

METHODS

Sample preparation. High-quality single crystals of $SrCo_2V_2O_8$ were grown using the floating-zone method. Crystal structure and magnetic properties were characterized by X-ray diffraction, neutron diffraction and magnetization measurements[22]. For the optical experiments, single crystals were oriented using X-ray Laue diffraction and cut perpendicular to the tetragonal c axis with a typical surface area of 4 mm × 4 mm and a thickness of 1 mm.

Terahertz spectroscopy in magnetic fields. Low-frequency optical experiments were carried out in Augsburg. For the transmission spectroscopy below 1 THz, backward wave oscillators were used as tunable sources of electromagnetic waves. A magneto-optic cryostat (Oxford Instruments/Spectromag) was used to apply external magnetic fields up to 7 T and to control temperatures down to 2 K. High-field optical measurements were performed in the High Field Magnet Laboratory in Nijmegen. Transmission spectra were measured using a Fourier-transform spectrometer Bruker IFS-113v, combined with a 30-tesla Bitter electromagnet. Terahertz electromagnetic waves were generated by a Mercury lamp and detected by a silicon bolometer. For all optical measurements, the external magnetic fields were applied parallel to the crystallographic c axis (longitudinal field $B \parallel c$) and to the propagation direction of the electromagnetic wave (Faraday configuration $B \parallel k$).

Crystal and magnetic structure of $SrCo_2V_2O_8$. The spin-1/2 Heisenberg–Ising antiferromagnetic chain system $SrCo_2V_2O_8$ crystallizes in a tetragonal structure with space group $I4_1cd$ (Extended Data Fig. 1) and lattice constants $a = 12.2710(1)$ Å and $c = 8.4192(1)$ Å at room temperature. The screw-chain structure is based on edge-shared CoO_6 octahedra. The screw axis of every chain is along the crystallographic c direction with a period of four Co^{2+} ions (Extended Data Fig. 1a). In each unit cell, there are four chains, two with left-handed screw axes and two with right-handed ones (Extended Data Fig. 1b). The leading inter-chain couplings are between Co^{2+} ions from the neighbouring chains with the same chirality[32,33], as indicated in Extended Data Fig. 1b. Compared to the intra-chain interaction, the inter-chain coupling is almost negligible, $J_\perp/J < 10^{-2}$ (refs 32, 33). Owing to crystal-field effects and spin–orbit coupling, the atomic magnetic moments of each Co^{2+} ion form a ground state of Kramers doublets corresponding to the total angular momentum of 1/2, which comprises spin and orbital degrees of freedom. According to crystal-field theory[21,34] and electron spin-resonance measurements[23], the magnetic gap between the two lower-lying Kramers doublets is about 22 meV. The nearest-neighbour exchange interactions between the Kramers doublets in the ground state (corresponding to $m_J = \pm 1/2$) can be described by the spin-1/2 Heisenberg–Ising antiferromagnetic model. Below $T_N \approx 5$ K, a Néel-ordered phase is stabilized in zero magnetic field[22].

High-field magnetization in $SrCo_2V_2O_8$. Magnetization measurements were performed at the Dresden High Magnetic Field Laboratory in a pulsed magnetic field up to 60 T. Extended Data Fig. 2a shows the magnetization in a longitudinal field $B \parallel c$ at 1.7 K. The magnetization curve exhibits distinct features in different phases and a clear signature of a quantum phase transition. At zero magnetic field, the Néel-ordered phase is characterized by gapped fractional spinon excitations. A clear onset of magnetization occurs at $B_c = 4$ T, indicating the phase transition to the one-dimensional gapless phase (critical regime). Slightly above B_c, the magnetization increases quasi-linearly, and then strongly nonlinearly above 10 T. This behaviour is also reflected in the field derivative of the magnetization, dM/dH: a nearly constant value is followed by an evident upturn at higher fields (Extended Data Fig. 2b). Field-induced phase transitions at B_c and B_s are evidenced by the anomalies in the field derivative of magnetization. Above $B_s = 28.7$ T, the spins are fully field-polarized and the system enters a field-induced ferromagnetic phase with saturated magnetization. We use the spin-1/2 Heisenberg–Ising antiferromagnetic model (equation (1)) to simulate the field dependence of the magnetization in the gapless one-dimensional critical regime between B_c and B_s (ref. 2). Using the same parameters as determined from the excitation spectra ($J = 3.55$ meV, $g_\parallel = 6.2$ and $\Delta = 2$; Fig. 4), we can describe the experimental magnetization curve quite well.

Low-energy phonon spectrum in $SrCo_2V_2O_8$. The low-energy phonon reflection spectrum was measured using Fourier-transform infrared spectroscopy. Extended Data Fig. 3 shows the phonon spectra of $SrCo_2V_2O_8$ measured for the polarization $E^\omega \parallel a$ in the relevant spectral range. The strong reflection due to phonon excitations from 8 meV to 13.5 meV strongly reduces the transmission at the corresponding spectral range.

Bethe-ansatz formalism. We use the Bethe ansatz to obtain the eigenenergies and eigenwavefunctions of the one-dimensional spin-1/2 antiferromagnetic Heisenberg–Ising model:

$$H(\Delta, h) = J \sum_{n=1}^{N} [(S_n^x S_{n+1}^x + S_n^y S_{n+1}^y) + \Delta S_n^z S_{n+1}^z] - h \sum_{n=1}^{N} S_n^z \quad (1)$$

in which $\Delta > 1$ accounts for the Ising anisotropy in $SrCo_2V_2O_8$ (refs 23, 24) and h is related to the external magnetic field B by $h \equiv g_\parallel \mu_B B$. The Hamiltonian in equation (1) reduces to the isotropic Heisenberg model for $\Delta = 1$, whereas for the model with easy-plane anisotropy, $0 < \Delta < 1$. The dynamical properties of this model have been studied extensively in various regimes[1–11,26,35–38]. Here, we follow an established theoretical approach[6,35] to solve the Heisenberg–Ising model, and focus on the comparison with the experimental results in $SrCo_2V_2O_8$. Details of the theoretical methods and results are presented in ref. 26.

Starting from the fully polarized state as the reference state, we can divide the states into subspaces according to the number of flipped spins r, or equivalently the total spin in the z direction $S_T^z = N/2 - r$. The corresponding wavefunctions are obtained by solving the Bethe-ansatz equations[35]

$$N\theta_1(\lambda_j) = 2\pi I_j + \sum_{l=1}^{r} \theta_2(\lambda_j - \lambda_l), \quad j = 1, \dots, r$$

in which $\theta_1(\lambda)$ and $\theta_2(\lambda)$, as functions of rapidity λ, are defined by

$$\theta_n(\lambda) \equiv 2\arctan\left[\frac{\tan(\lambda)}{\tanh(n\eta/2)}\right] + 2\pi \left\lfloor \frac{\mathrm{Re}(\lambda)}{\pi} + \frac{1}{2} \right\rfloor$$

where $\lfloor A \rfloor$ denotes the floor function, which gives the greatest integer not larger than A.

The Bethe quantum numbers $\{I_j\}, j \in \{1, \dots, r\}$, take integer values when r is odd and half-integer values when r is even (see following sections). A state is called a real Bethe eigenstate (psinon or antipsinon) if all of the rapidities λ_j are real and a string state if there is a complex-valued λ_j.

A schematic of the distribution of ground-state Bethe quantum numbers is shown in Extended Data Fig. 4a for $N = 32$ and $S_T^z = 8$. The low-lying excitations of real Bethe states can be classified according to either one of the two patterns that have purely real rapidities $\{\lambda_j\}, j \in \{1, \dots, r\}$ (refs 4, 6–10, 35): n-pair psinon–psinon states ($n\psi\psi$) and n-pair psinon–antipsinon states ($n\psi\psi^*$). The Bethe quantum numbers of an $n\psi\psi$ state can be produced by first extending the left (right) edge of the ground-state Bethe quantum numbers further to the left (right) by n, then removing $2n$ numbers within the extended range. Those of an $n\psi\psi^*$ state can be obtained by removing n numbers in the ground-state range and putting them outside the range. Illustrations of the two situations are shown in Extended Data Fig. 4b and c for $1\psi\psi$ and $1\psi\psi^*$, respectively. Extended Data Fig. 4d shows the Bethe quantum numbers of a string state, which has larger energy than the real Bethe states.

Transverse dynamic structure factors. The dynamic structure factors (DSFs) relevant to the experiment are calculated for Ising anisotropy $\Delta = 2$ and system size $N = 200$ using the determinant formulas in the algebraic Bethe-ansatz formalism[6]. Extended Data Fig. 5 displays the results of $S^{-+}(q, \omega)$ and $S^{+-}(q, \omega)$ at a representative magnetization $2m = 0.4$ (ref. 26). $S^{-+}(q, \omega)$ is dominated by gapless continua that are formed by $1\psi\psi$ and $2\psi\psi$ excitations, whereas in $S^{+-}(q, \omega)$ there are several well-separated dynamical branches. For $S^{+-}(q, \omega)$, the lowest-lying gapless continua are formed by $1\psi\psi^*$ and $2\psi\psi^*$ excitations. The corresponding spectral weights are located mainly in the energy range $\hbar\omega < 3J$. The higher-energy separated continua correspond to two-string and three-string excitations that are found in the spectral ranges $\hbar\omega > 3J$ and $\hbar\omega > 5J$, respectively.

The momentum-integrated sum rules. By rescaling $S^\pm$ to $S^\pm/\sqrt{2}$, the momentum-integrated sum rules can be expressed as

$$R_{a\bar{a}} = \frac{1}{N} \sum_q \int_0^\infty \frac{S^{a\bar{a}}(q, \omega)}{2\pi} d\omega = \frac{1}{4} + \frac{m}{2} c_a$$

where $c_a = \pm 1$ for $a = \pm$, respectively.

To evaluate the saturation levels of the sum rules, we define the ratio

$$\nu_{a\bar{a}} = \frac{R'_{a\bar{a}}}{R_{a\bar{a}}}$$

where $R'_{a\bar{a}}$ is calculated from a partial summation over the selected excitations.

Ratio of the momentum-integrated intensity of transverse DSFs. The ratios of momentum-integrated intensity for S^{+-} and S^{-+} are displayed in Extended Data Fig. 6a and b, respectively, The calculations are carried out for $2m$ varied from 0.1 to 0.9 with steps of 0.1 (ref. 26). The good saturations of sum rules (above 87%) for both S^{+-} and S^{-+} over the entire range of magnetization indicate that most of the spectral weights are accounted for in the calculations. Particularly for S^{+-}, the string excitations, and especially the three-string states, become progressively important when magnetization is lowered. Hence, the string states have a predominant role in the dynamical properties in the low-magnetization region.

Comparison between theory and experiment. With the four-fold screw axis (Extended Data Fig. 1a), the Brillouin zone is folded by a factor of four in $SrCo_2V_2O_8$; thus, as well as those at $q = 0$, the excitations at $q = \pi$ and $q = \pi/2$ should also be considered for comparison to the terahertz experiments. On the basis of the results shown in Extended Data Fig. 5, in the following we present a detailed analysis of the magnetic-field-dependent properties of the various excitations for these momenta.

Extended Data Figs 7–10 show the DSFs for psinon–psinon, psinon–antipsinon, two-string and three-string excitations, respectively, as functions of energy for magnetizations $2m = 0.1$–0.9 and $q = 0$, $q = \pi/2$ and $q = \pi$.

As shown in Extended Data Fig. 7, for the psinon–psinon excitations the DSF spectra exhibit very sharp peaks, and the peak positions shift with magnetic field (or magnetization) only for $q = \pi/2$. By contrast, at $q = 0$ and $q = \pi$ the excitations form continua in the whole spectral range $(2J)$, and we cannot define peak positions, or the peak positions are almost independent of magnetic field. Thus, we can clearly distinguish the psinon–psinon excitations at $q = \pi/2$ from those at $q = 0$ and $q = \pi$. Moreover, the softening of the $q = \pi/2$ modes upon increasing magnetic fields is in clear contrast to the hardening of the other types of excitation (see Fig. 4). This is because psinon–psinon excitations correspond to flipping one spin parallel to the magnetic field. Indeed, the psinon–psinon excitations at $q = \pi/2$ are observed by our terahertz spectroscopy (see Fig. 4).

The psinon–antipsinon excitations exhibit very sharp peaks at $q = 0$ and $q = \pi/2$, but form continua at $q = \pi$ (see Extended Data Fig. 8). At $q = 0$, we can clearly see the peaks in the whole field range (Extended Data Fig. 8a), whereas for $q = \pi/2$ peaks are well resolved only above half-magnetization saturation (Extended Data Fig. 8b). For both of the modes, the peak positions shift to higher energy with increasing magnetic field. The psinon–antipsinon excitations at $q = 0$ are observed experimentally for all magnetic fields above $B_c = 4$ T (see Fig. 4), whereas those at $q = \pi/2$, which appear above the field corresponding to half-saturated magnetization, $B_{hs} = 25$ T and at low energies, are yet to be found. The extended continua at $q = \pi$ are strongly overlapping for different magnetic fields, and so they cannot be resolved by the present magneto-optical spectroscopy.

Extended Data Fig. 9 shows the DSFs of two-string excitations. At $q = \pi$ the spectra exhibit sharp peaks with well-defined peak positions, whereas at $q = 0$ the peaks are relatively broad. With increasing magnetic fields, these two modes are evidently hardening and so can readily be identified. By contrast, the continua at $q = \pi/2$ overlap with each other for different magnetic fields. Therefore, only at $q = \pi$ and $q = 0$ can the two-string excitations be observed experimentally (see Fig. 4).

The three-string excitations form extended continua at $q = 0$ and $q = \pi$, which overlap for the different magnetic fields, as shown in Extended Data Fig. 10. By contrast, at $q = \pi/2$ the excitation spectra exhibit well-defined peaks with peak positions shifting to higher energy with increasing magnetic field. This mode can clearly be identified experimentally (see Fig. 4).

To summarize, only the excitations with well-defined peak positions that shift evidently with magnetic fields can be resolved, as have been observed for R_0, $R_{\pi/2}$, $\chi_0^{(2)}$, $\chi_\pi^{(2)}$ and $\chi_\pi^{(3)}$ by our magneto-optic terahertz spectroscopy (see Fig. 4). By contrast, the other excitations form continua in a broad spectral range and cannot easily be resolved by the terahertz spectroscopy. The theoretical peak positions of the excitations R_0, $R_{\pi/2}$, $\chi_0^{(2)}$, $\chi_\pi^{(2)}$ and $\chi_{\pi/2}^{(3)}$ are plotted as functions of magnetic field and compared to the experimental results. We fix the exchange interaction and Ising anisotropy to the previously determined values for $SrCo_2V_2O_8$, $J = 3.55$ meV and $\Delta = 2$ (ref. 24), and with g-factor $g_\parallel = 6.2$ all five experimentally observed modes can be very well described by the theory, as presented in Fig. 4.

Data availability. The data that support the findings of this study are available from the corresponding author on reasonable request.

32. Grenier, B. *et al.* Longitudinal and transverse Zeeman ladders in the Ising-like chain antiferromagnet BaCo₂V₂O₈. *Phys. Rev. Lett.* **114,** 017201 (2015).
33. Bera, A. *et al.* Spinon confinement in a quasi-one dimensional anisotropic Heisenberg magnet. *Phys. Rev. B* **96,** 054423 (2017).
34. Shiba, H., Ueda, Y., Okunishi, K., Kimura, S. & Kindo, K. Exchange interaction via crystal-field excited states and its importance in CsCoCl₃. *J. Phys. Soc. Jpn* **72,** 2326–2333 (2003).
35. Takahashi, M. *Thermodynamics of One-Dimensional Solvable Models* (Cambridge Univ. Press, 2005).
36. Caux, J.-S. & Maillet, J. M. Computation of dynamical correlation functions of Heisenberg chains in a magnetic field. *Phys. Rev. Lett.* **95,** 077201 (2005).
37. Pereira, R. G., White, S. R. & Affleck, I. Exact edge singularities and dynamical correlations in spin-1/2 chains. *Phys. Rev. Lett.* **100,** 027206 (2008).
38. He, F., Jiang, Y.-Z., Yu, Y.-C., Lin, H.-Q. & Guan, X.-W. Quantum criticality of spinons. *Phys. Rev. B* **96,** 220401(R) (2017).

a

Néel ordered

b
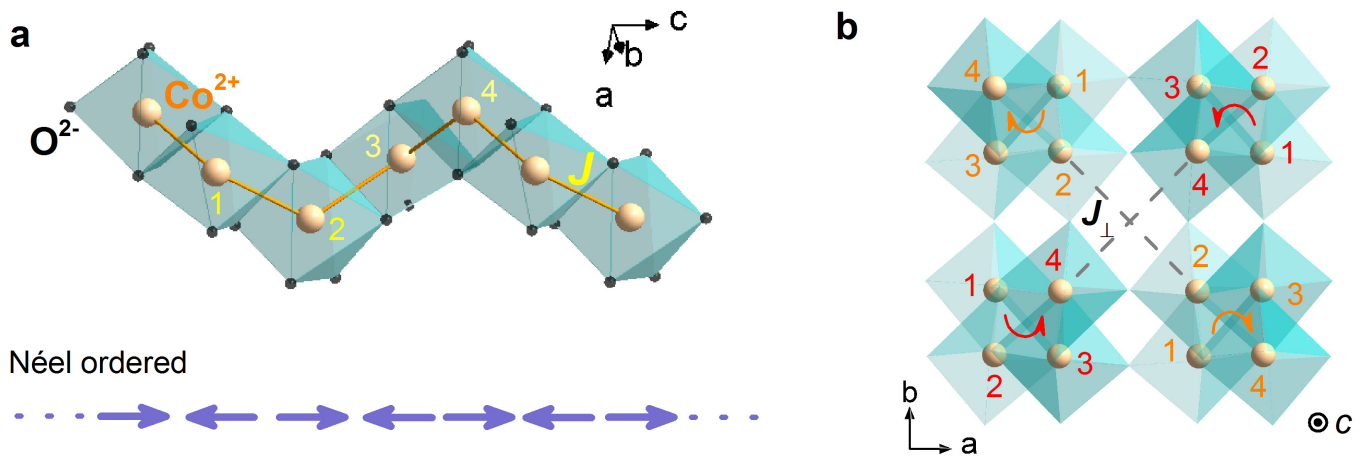
Extended Data Figure 1 | Crystal and magnetic structure of SrCo$_2$V$_2$O$_8$.
a, The screw-chain structure consists of edge-shared CoO$_6$ octahedra. Each chain has screw-axis symmetry with a period of four Co^{2+} ions (as numbered by the integers 1, 2, 3 and 4), corresponding to the lattice constant along the c axis. The Néel-ordered phase is illustrated by antiparallel arrows representing magnetic moments at the Co^{2+} sites. Intra-chain nearest-neighbour interaction is denoted by J. **b**, Viewing from the c axis, each unit cell contains four screw chains with left- or right-handed screw axes. The leading inter-chain coupling $J_\perp$ is indicated, which is between the Co^{2+} ions in the same layer (denoted by the same integer as the Co site) and from chains with the same chirality. It is very small compared to the intra-chain interaction, $J_\perp/J < 10^{-2}$ (refs 32, 33).
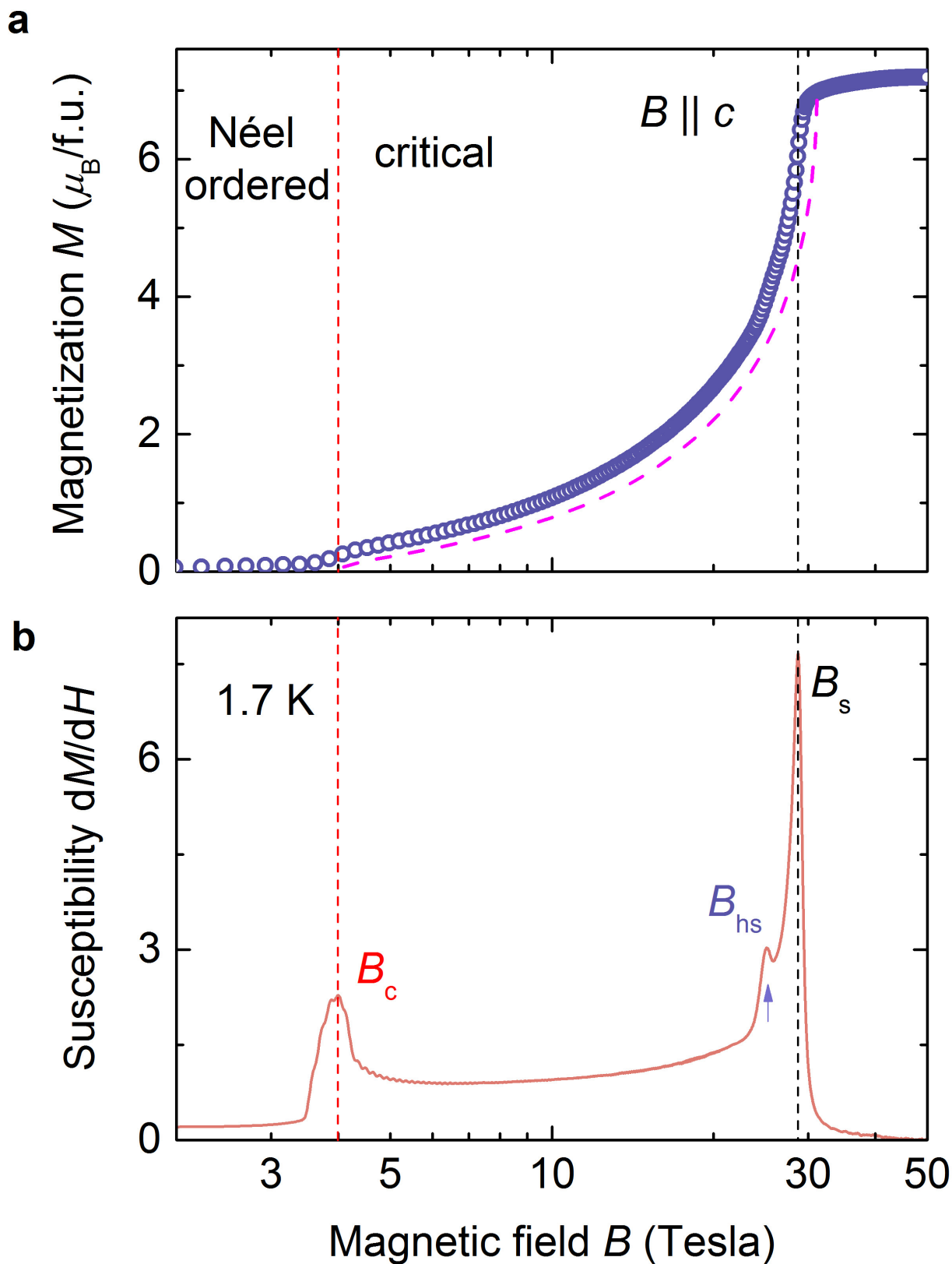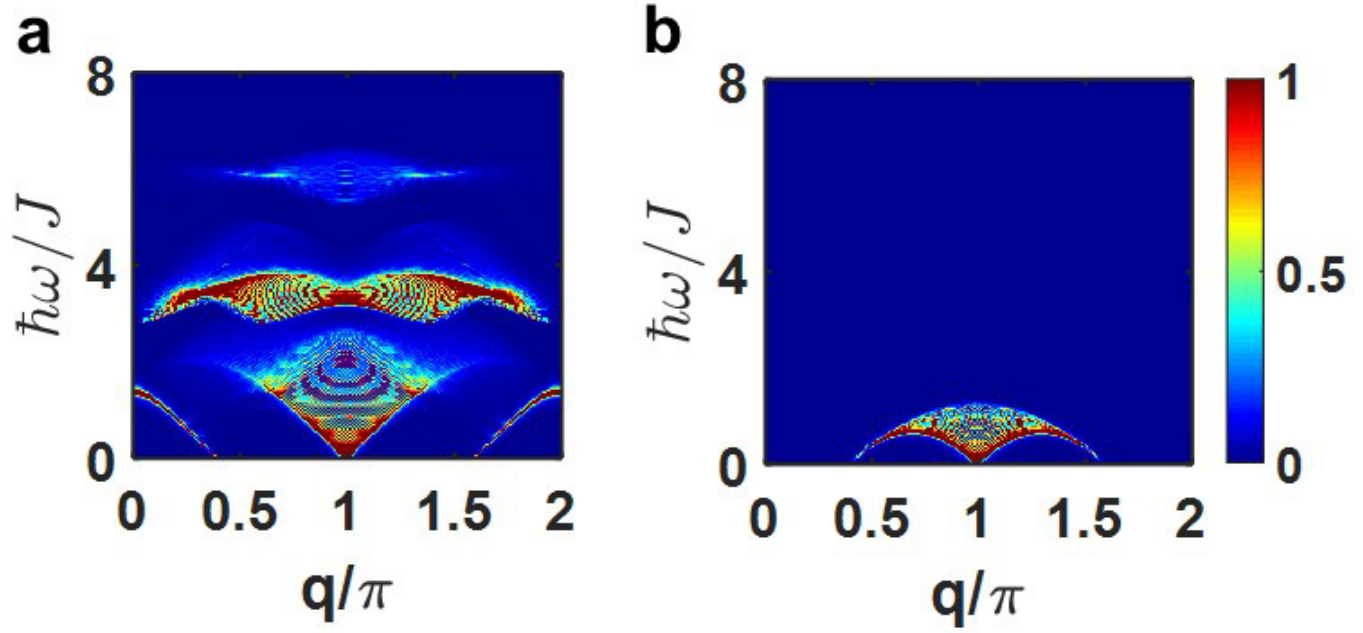
Extended Data Figure 2 | High-field magnetization and magnetic susceptibility of SrCo$_2$V$_2$O$_8$. a, Magnetization M as a function of an applied longitudinal magnetic field B along the Ising axis ($B \parallel c$), measured at 1.7 K (circles). Theoretical magnetization of the Heisenberg–Ising chain model is shown by the dashed line. **b**, Magnetic susceptibility dM/dH as a function of the applied longitudinal field B. A quantum phase transition from the Néel-ordered phase to the critical phase is revealed by the onset of magnetization and the peak in the susceptibility curve at the critical field $B_c = 4$ T. Saturated magnetization is observed above the field $B_s = 28.7$ T and indicated by the sharp peak in the susceptibility. The small anomaly at $B_{hs} = 25$ T seen in the susceptibility is close to the field of half-saturated magnetization.
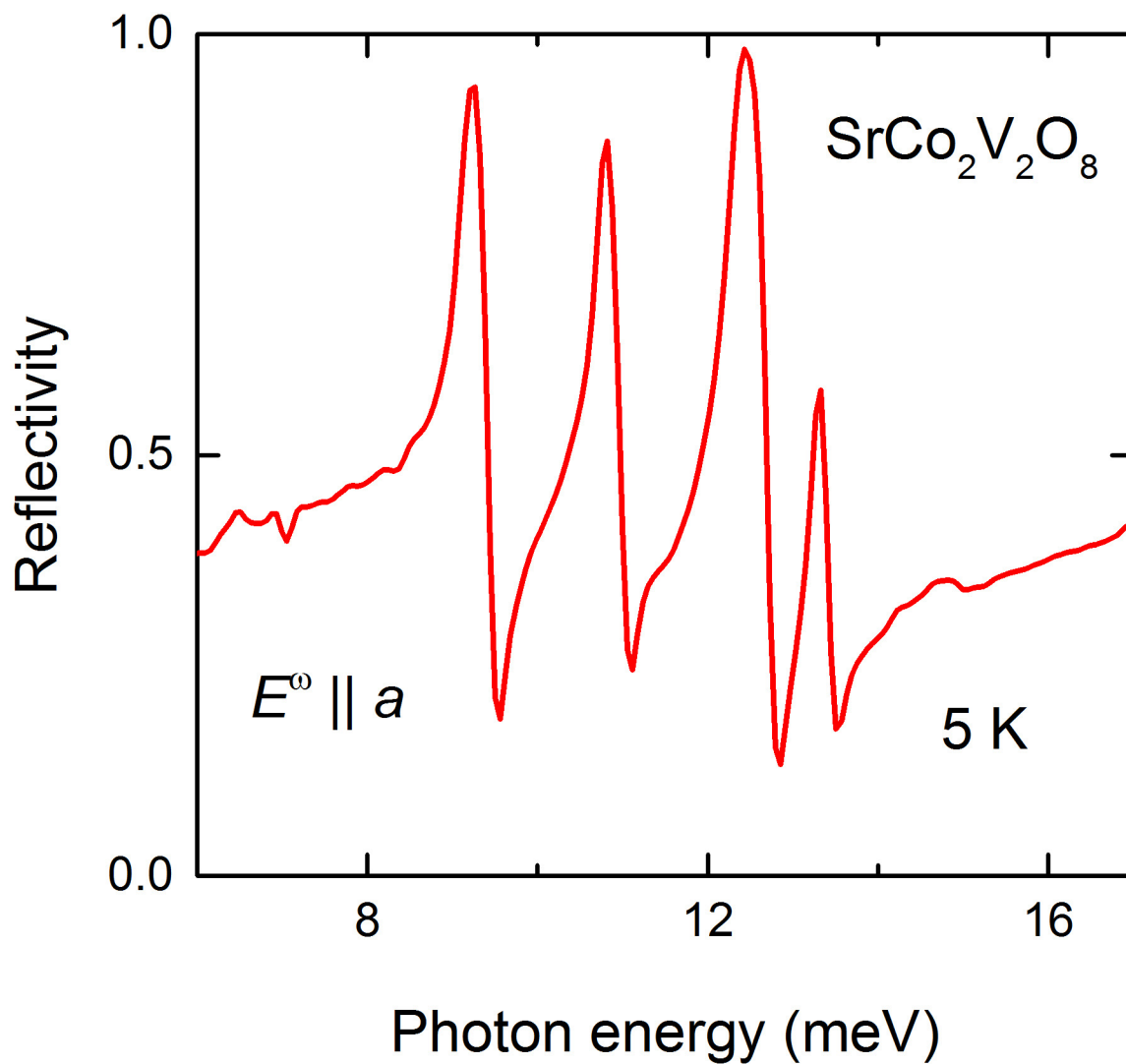
Extended Data Figure 3 | Low-energy phonon spectrum of SrCo$_2$V$_2$O$_8$. The phonon spectra of SrCo$_2$V$_2$O$_8$ measured for the polarization $E^\omega \parallel a$ at 5 K. Strong reflectivity due to phonon excitations is observed in the spectral range 8–13.5 meV.

Extended Data Figure 4 | Schematics of patterns of Bethe quantum numbers. a, The ground state. **b**, One-pair psinon–psinon state $1\psi\psi$. **c**, One-pair psinon–antipsinon state $1\psi\psi^{*}$. **d**, Length-two string state $1\chi^{(2)}R$. The system size is taken as $N = 32$ and the magnetization is $S_{\mathrm{T}}^{z} = 8$.

Extended Data Figure 5 | DSFs. a, b, $S^{+-}(q, \omega)$ and $S^{-+}(q, \omega)$, respectively, as functions of energy $\hbar\omega/J$ (vertical axis) and momentum q/π (horizontal axis) for $2m = 0.4$ and $N = 200$. The gapless continua are formed by rea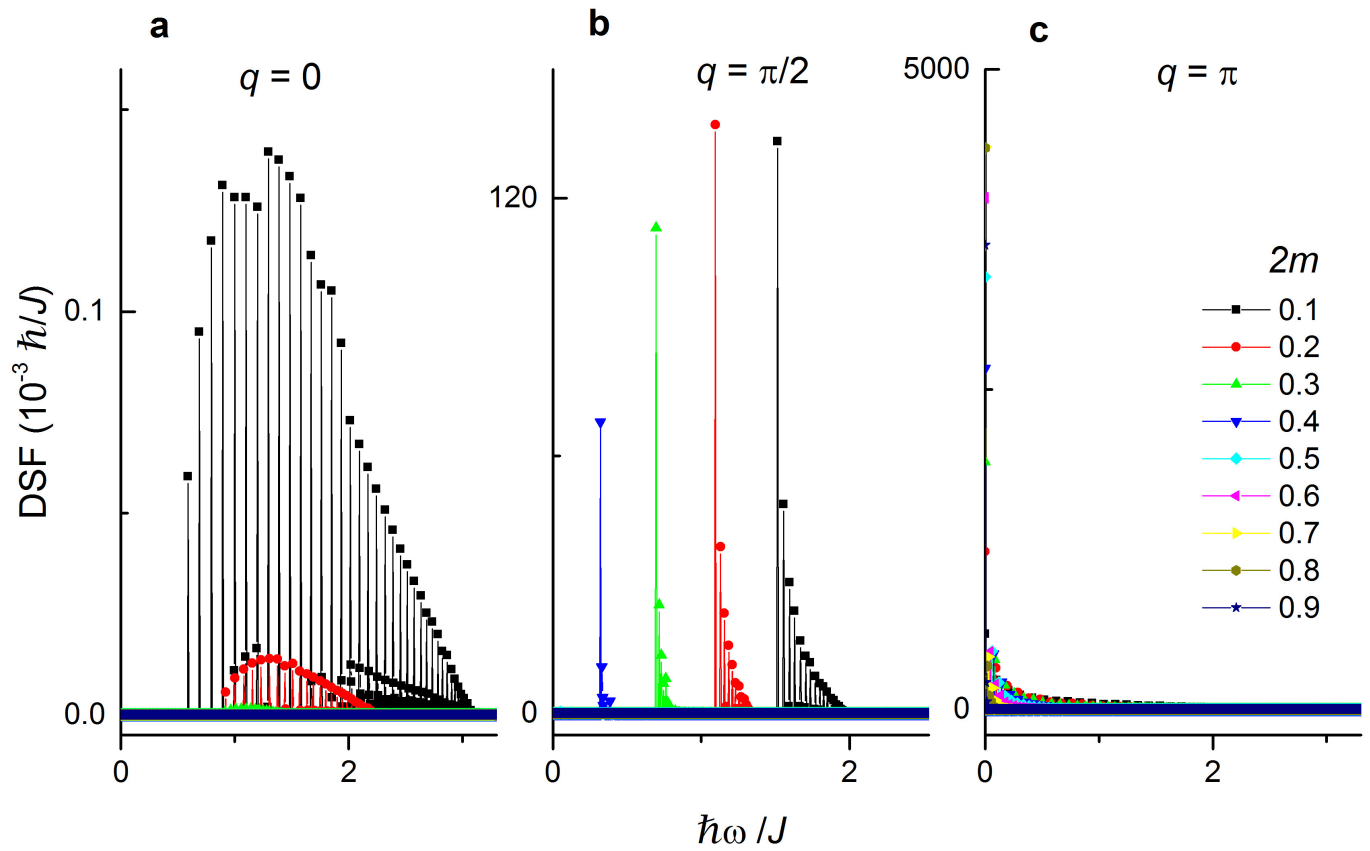l Bethe eigenstates (psinon–antipsinon pairs in S^{+-} and psinon–psinon pairs in S^{-+}). For S^{+-} (**a**), the higher-energy continua correspond to excitations of two-string ($\hbar\omega > 3J$) and three-string ($\hbar\omega > 5J$) states.
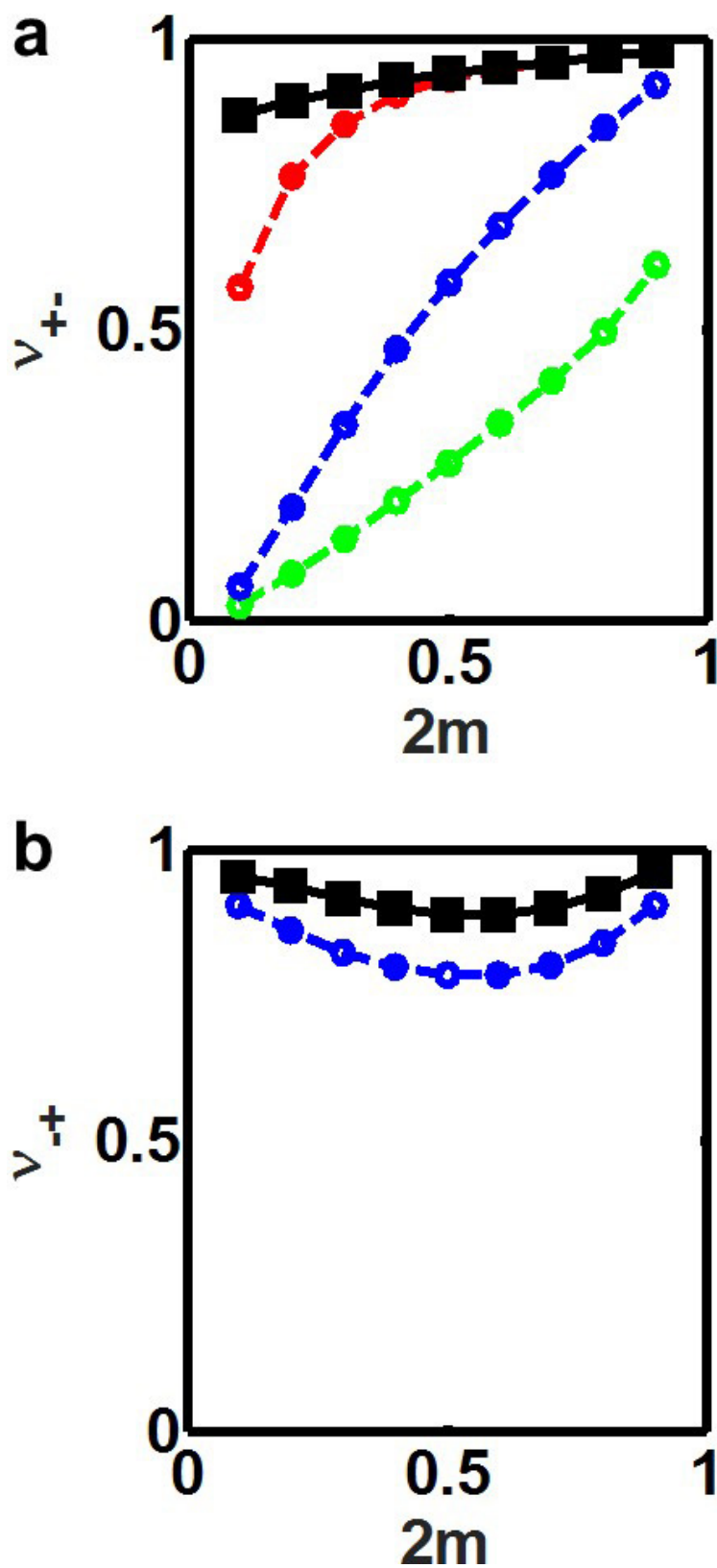
Extended Data Figure 6 | The momentum-integrated ratios. a, b, ν_{+-} for S^{+-} and ν_{-+} for S^{-+}, respectively, as functions of magnetization $2m$. In **a**, the green line is the $1\psi\psi^*$ contribution. The blue, red and the black lines are augmented by progressively taking into account the $2\psi\psi^*$, two-string and three-string contributions, respectively. In **b**, the blue and black lines represent the $1\psi\psi$ and $1\psi\psi + 2\psi\psi$ contributions, respectively.
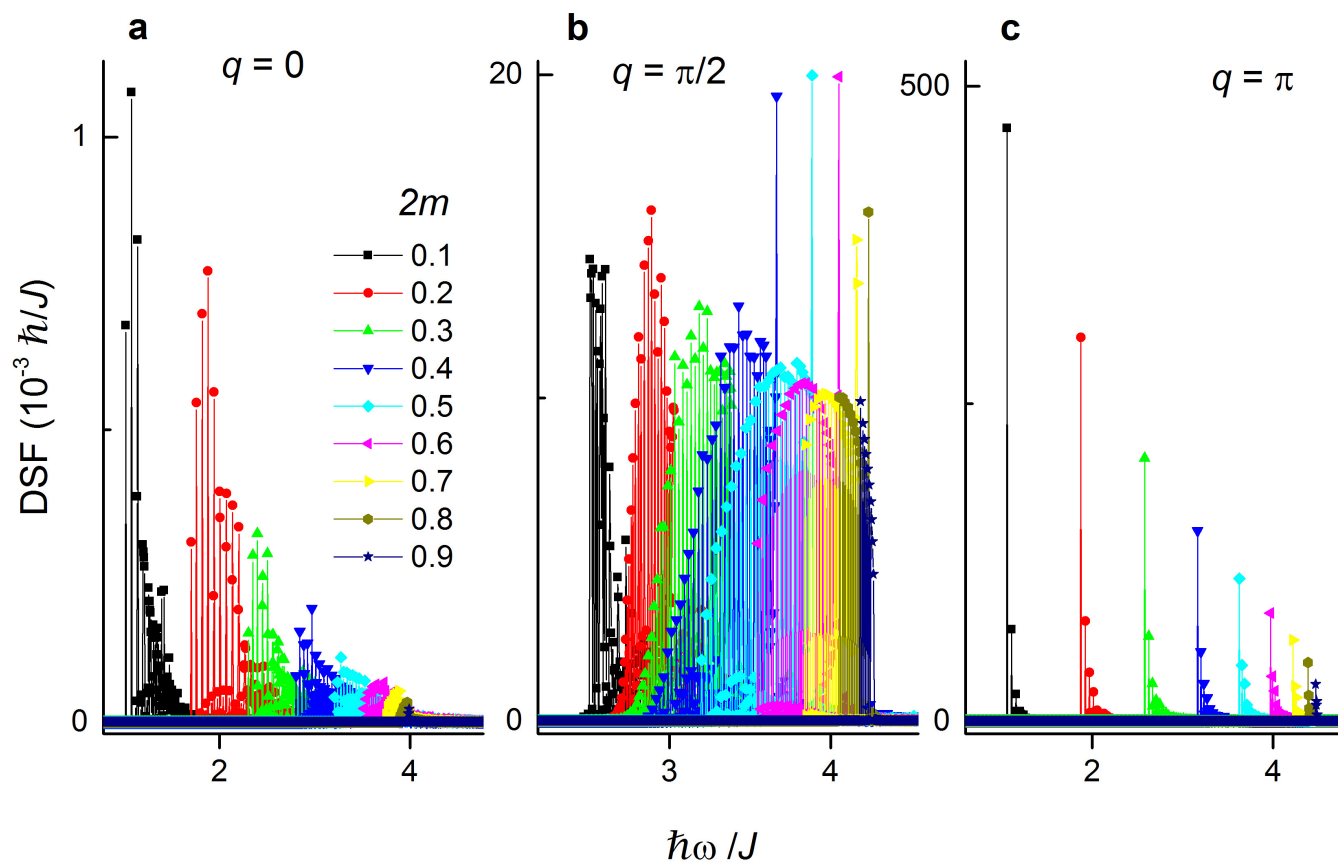
psinon-psinon pairs

a $q = 0$

b $q = \pi/2$

c $q = \pi$

DSF ($10^{-3}\ \hbar/J$)

0.1

0.0

5000

120

0

0

$\hbar\omega\,/J$

0

2

0

2

0

2

2m
- ■ 0.1
- ● 0.2
- ▲ 0.3
- ▼ 0.4
- ◆ 0.5
- ◄ 0.6
- ► 0.7
- ● 0.8
- ★ 0.9

Extended Data Figure 7 | DSF of psinon–psinon pairs as a function of energy for 2m = 0.1–0.9. a, $q = 0$; **b**, $q = \pi/2$; **c**, $q = \pi$.
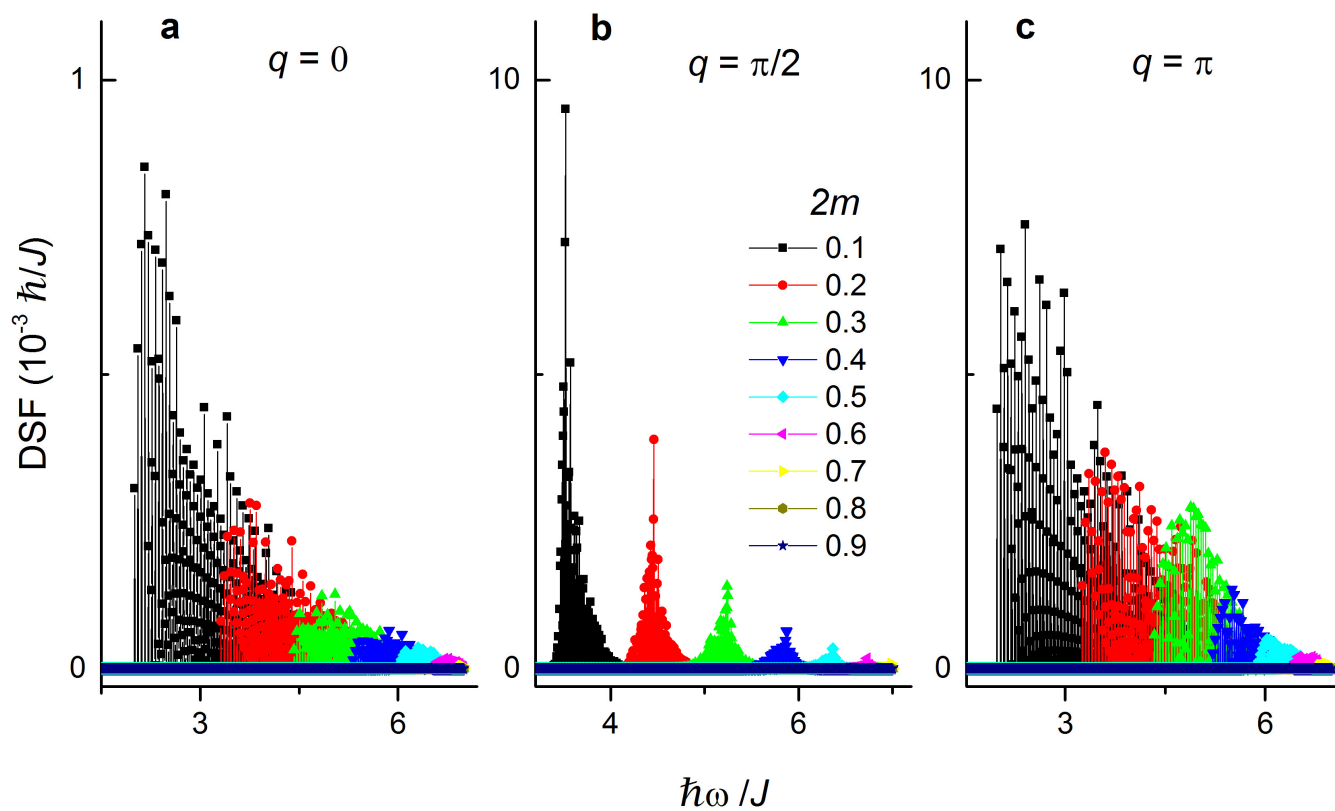
psinon-antipsinon pairs
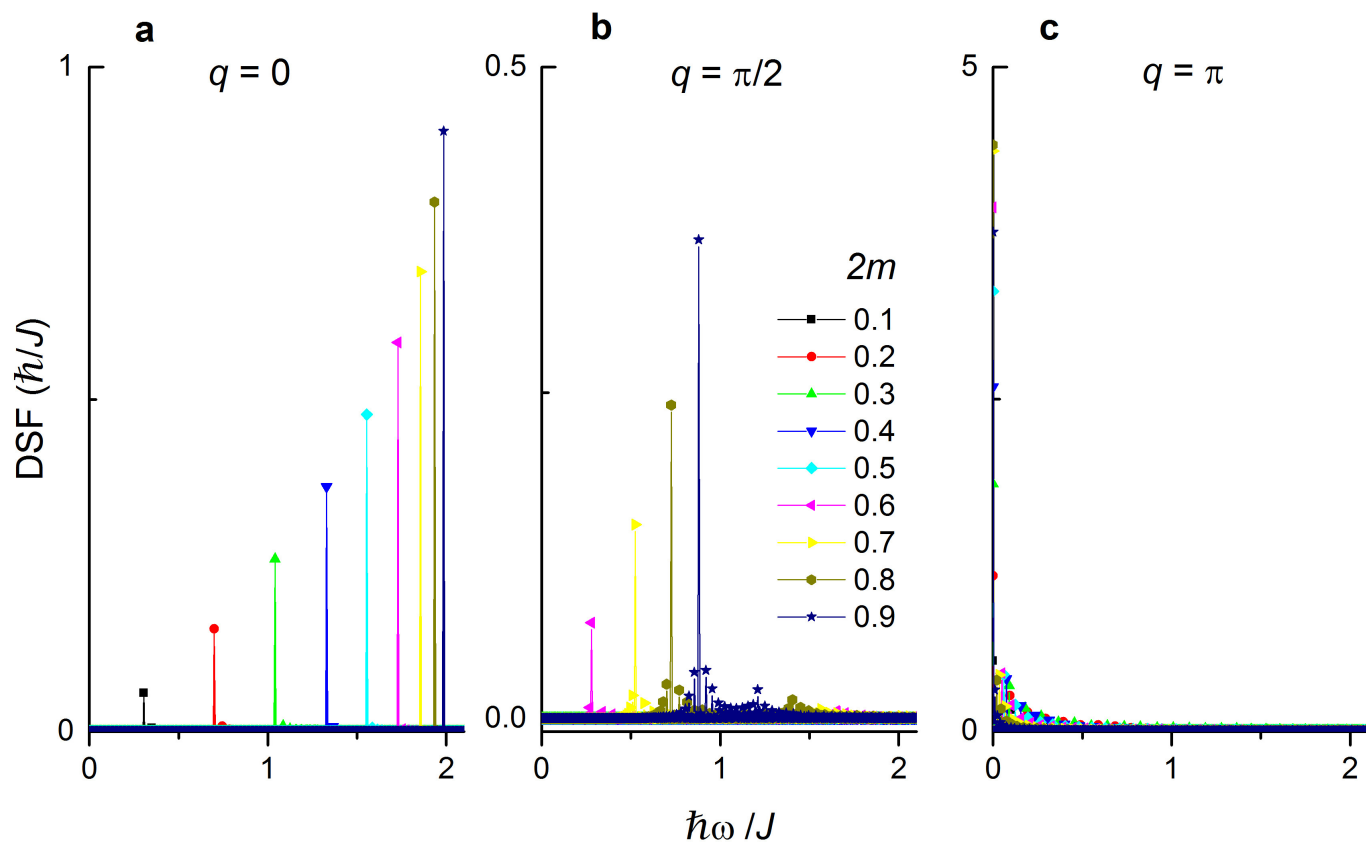
Extended Data Figure 8 | DSF of psinon–antipsinon pairs as a function of energy for 2*m* = 0.1–0.9. a, *q* = 0; **b**, *q* = π/2; **c**, *q* = π.

2-string $\chi_q^{(2)}$

a $q = 0$

b $q = \pi/2$

c $q = \pi$

DSF (10^{-3} $\hbar/J$)

$\hbar\omega /J$

Extended Data Figure 9 | DSF factor of two-string states as a function of energy for 2m = 0.1–0.9. a, $q = 0$; **b**, $q = \pi/2$; **c**, $q = \pi$.

3-string $\chi_q^{(3)}$

Extended Data Figure 10 | DSF of three-string states as a function of energy for 2m = 0.1–0.9. a, $q = 0$; **b**, $q = \pi/2$; **c**, $q = \pi$.